ADVANCED MATERIALS
www.advmat.de

Bioresorbable Multilayer Organic–Inorganic Films for Bioelectronic Systems

Ziying Hu, Hexia Guo, Dongqi An, Mingzheng Wu, Anika Kaura, Hannah Oh, Yue Wang, Mengjia Zhao, Shuo Li, Quansan Yang, Xudong Ji, Shupeng Li, Bo Wang, Davin Yoo, Phuong Tran, Nayereh Ghoreishi-Haack, Yevgenia Kozorovitskiy, Yonggang Huang, Rui Li, and John A. Rogers**

Bioresorbable electronic devices as temporary biomedical implants represent an emerging class of technology relevant to a range of patient conditions currently addressed with technologies that require surgical explantation after a desired period of use. Obtaining reliable performance and favorable degradation behavior demands materials that can serve as biofluid barriers in encapsulating structures that avoid premature degradation of active electronic components. Here, this work presents a materials design that addresses this need, with properties in water impermeability, mechanical flexibility, and processability that are superior to alternatives. The approach uses multilayer assemblies of alternating films of polyanhydride and silicon oxynitride formed by spin-coating and plasma-enhanced chemical vapor deposition , respectively. Experimental and theoretical studies investigate the effects of material composition and multilayer structure on water barrier performance, water distribution, and degradation behavior. Demonstrations with inductor-capacitor circuits, wireless power transfer systems, and wireless optoelectronic devices illustrate the performance of this materials system as a bioresorbable encapsulating structure.

1. Introduction

Bioresorbable electronics are an emerging class of advanced electronic systems that can completely dissolve to environmentally and biologically benign byproducts after desired functional lifetimes, ranging from days to months.[1–3] For consumer or industrial applications, this characteristic feature eliminates solid electronic waste and difficulties related to its management; in biomedical implants, resorption reduces risks and costs associated with extraction surgeries.[1,4–7] Previous demonstrations of this technology include systems for continuous physiological recording,[8] electrophysiological monitoring,[9] electrotherapy,[2,10] and drug delivery.[11] A critical engineering challenge for these and related types of devices is in encapsulation materials that

Z. Hu, H. Guo, M. Wu, Y. Wang, S. Li, Q. Yang, J. A. Rogers
Querrey Simpson Institute for Bioelectronics
Northwestern University
Evanston, IL 60208, USA
E-mail: jrogers@northwestern.edu

H. Guo, M. Zhao, D. Yoo, J. A. Rogers
Department of Materials Science and Engineering
Northwestern University
Evanston, IL 60208, USA

D. An, B. Wang, R. Li
State Key Laboratory of Structural Analysis
Optimization and CAE Software for Industrial Equipment
Department of Engineering Mechanics
and International Research Center for Computational Mechanics
Dalian University of Technology
Dalian 116024, P. R. China
E-mail: ruili@dlut.edu.cn

The ORCID identification number(s) for the author(s) of this article can be found under https://doi.org/10.1002/adma.202309421

DOI: 10.1002/adma.202309421

M. Wu, H. Oh, Y. Kozorovitskiy
Department of Neurobiology
Northwestern University
Evanston, IL 60208, USA

A. Kaura, Y. Wang, X. Ji, J. A. Rogers
Department of Biomedical Engineering
Northwestern University
Evanston, IL 60208, USA

Q. Yang, S. Li, Y. Huang, J. A. Rogers
Department of Mechanical Engineering
Northwestern University
Evanston, IL 60208, USA

X. Ji
Simpson Querrey Institute
Northwestern University
Chicago, IL 60611, USA

P. Tran, N. Ghoreishi-Haack
Developmental Therapeutics Core
Northwestern University
Evanston, IL 60208, USA

J. A. Rogers
Department of Chemistry
Department of Neurological Surgery
Department of Electrical Engineering & Computer Science
Northwestern University
Evanston, IL 60208, USA

can provide barriers to surrounding biofluids but with degradation behaviors aligned to desired operational lifetimes. The difficulty is in balancing superior barrier performance with suitable degradation rates.

Materials commonly utilized for such purposes include organic polymer films, such as poly(lactic-co-glycolic acid) (PLGA),[12] polyanhydride (PA),[8,13] polyurethane (PU),[10] poly(octanediol citrate) (POC),[14] wax,[15] and cellulose,[16] and inorganic thin films, including monocrystalline silicon (mono-Si),[17] silicon dioxide (SiO_2),[9,18] silicon nitride (SiN_x),[9,19] and silicon oxynitrides (SiON).[20,21] Polymer materials are attractive due to their processability but they offer relatively poor barrier characteristics. Wax materials and PU have acceptable barrier characteristics but can require several years to completely degrade in vivo. Cellulose has some promise, but requires improvements in structure, processing, and barrier functionality.[16] Various inorganic alternatives offer superior properties. Thin films of mono-Si and thermally grown SiO_2 provide nearly perfect barriers, and their degradation proceeds by controlled processes of surface erosion.[17,22] The main disadvantage of these materials is that they involve high temperature synthesis procedures that must be conducted in controlled conditions, on narrow classes of substrates. Integration into bioresorbable electronic systems demands lift-off processes and transfer printing methods that can be difficult given the mechanical fragility of these materials. Plasma-enhanced chemical vapor deposition (PECVD) and other methods can be used to form inorganic thin films,[9,21,23] but previous studies of SiO_x, SiN_y, and SiON indicate that isolated defects and various forms of localized imperfections limit their fluid barrier performance.[20,22,24]

This work introduces classes of bioresorbable encapsulation materials that address these shortcomings by presenting a materials design strategy that allows imperfect inorganic barrier layers to meet specific application requirements. These systems consist of bioresorbable forms of PA and SiON configured into multilayer assemblies. Films of PA result from spin-coating a monomer solution followed by ultraviolet (UV)-initiated thiol-ene polymerization and those of SiON follow from deposition by PECVD. Alternating stacks of PA and SiON lead to tortuous paths and interface resistances for water permeation, and thus superior barrier properties. Experimental studies and theoretical simulations explore the interrelated effects of multilayer structure, chemical composition, water permeation characteristics, and degradation behaviors. These results provide evidence that multilayer SiON-PA films offer effective water barrier performance both in vitro and in vivo. Device level demonstrations with bioresorbable inductor–capacitor circuits, wireless power transfer systems, and wireless optoelectronic devices highlight practical applications of these multilayer SiON-PA films as encapsulating structures for bioelectronic devices.

2. Results

2.1. Preparation and Characterization of Bioresorbable Multilayer SiON-PA Films

The bioresorbable multilayer SiON-PA films reported here comprise a PA network, formed by the thiol-ene click chemistry, and SiON grown via PECVD (deposition temperature = 180 °C). Composition tunability of SiON during the PECVD process enables optimization of the degradation rate and mechanical properties (such as film stress). A substrate to provide mechanical support helps to avoid cracking of the SiON films under bending deformations. The substrate materials must offer good thermal stability, suitable mechanical properties, an appropriate degradation rate, low swelling ratio in an aqueous environment, low surface roughness, and strong interface adhesion with SiON. The PA network not only satisfies these requirements, but also offers transparency, enabling potential with optoelectronic devices.

Figure 1A shows the thiol-ene reaction between two alkyne monomers, 4-pentenoic anhydride (PEA) and 1,3,5-triallyl-1,3,5-triazine-2,4,6(1H,3H,5H)-trione (TTT), and two cross-linkers, pentaerythriol tetrakis(3-mercaptopropionate) (PETMP) and silsesquioxane (SSQ), as well as the degradation process associated with immersion of PA in water. The degradation mechanism of PA primarily involves bulk erosion and passive hydrolysis of the anhydride group, suggesting that the thickness of the PA film is unlikely to decrease significantly, but that the material will undergo weight loss over time.[25,26] The PA network refers to Ra-bSSQ-PA, where a is the molar ratio of PEA (anhydride monomer) to TTT and b is the molar percentage of the thiol group from SSQ. The amounts of anhydride groups (a) and SSQ (b) define the degradation, mechanical, and swelling properties.[27] Fourier-transform infrared spectroscopy (FTIR, Figure S1, Supporting Information) provides information on thiol groups (−SH) that react upon UV irradiation.[28] The results show that more than 97% of these groups react with alkyne monomers within 120 s for a 100-µm thick PA film (UV wavelength: 365 nm; intensity: 65 mW cm^{-2}). Thus, UV irradiation times are 150 and 30 s for PA films with thicknesses of 100 and 20 µm, respectively.

PA has good thermal stability, favorable mechanical properties, minimal swelling in aqueous environments, and suitable rates of degradation, as a substrate for films of SiON. Thermogravimetric analysis (TGA) indicates that PA (Ra-bSSQ-PA, a = 1, 2, and 3, and b = 0, 20, and 50) is stable below 310 °C (evaluated by 5% weight loss, Figure 1B). PA films are hydrophilic (Figure S2, Supporting Information)[29] and amorphous (differential scanning calorimetry (DSC), Figure S3A, Supporting Information) and their coefficients of thermal expansion (CTE) decrease with increasing SSQ content (Figure S3B, Supporting Information). The thermal properties indicate that PA can support deposition of SiON via PECVD at 180 °C. Dynamic mechanical analysis (DMA) of the stress–strain curves the fracture strains and the elastic moduli of films of PA (thicknesses: 100 µm), as Figure 1C and Figure S4 (Supporting Information). Incubating these films in phosphate-buffered saline (PBS) solution at 37 °C and comparing their dry and wet weights as a function of time defines aspects of degradation and swelling properties (Figure 1D and Figure S5, Supporting Information). The results suggest that increasing the amount of SSQ or decreasing that of anhydride groups improves the elastic modulus, reduces the degradation rate, and suppresses swelling. The composition of SiON is key to its water barrier properties and degradation.[20] X-ray photoelectron spectroscopy (XPS) shows that the atomic percentages of Si, O, and N in SiON grown by PECVD are 31.30%, 61.91%,

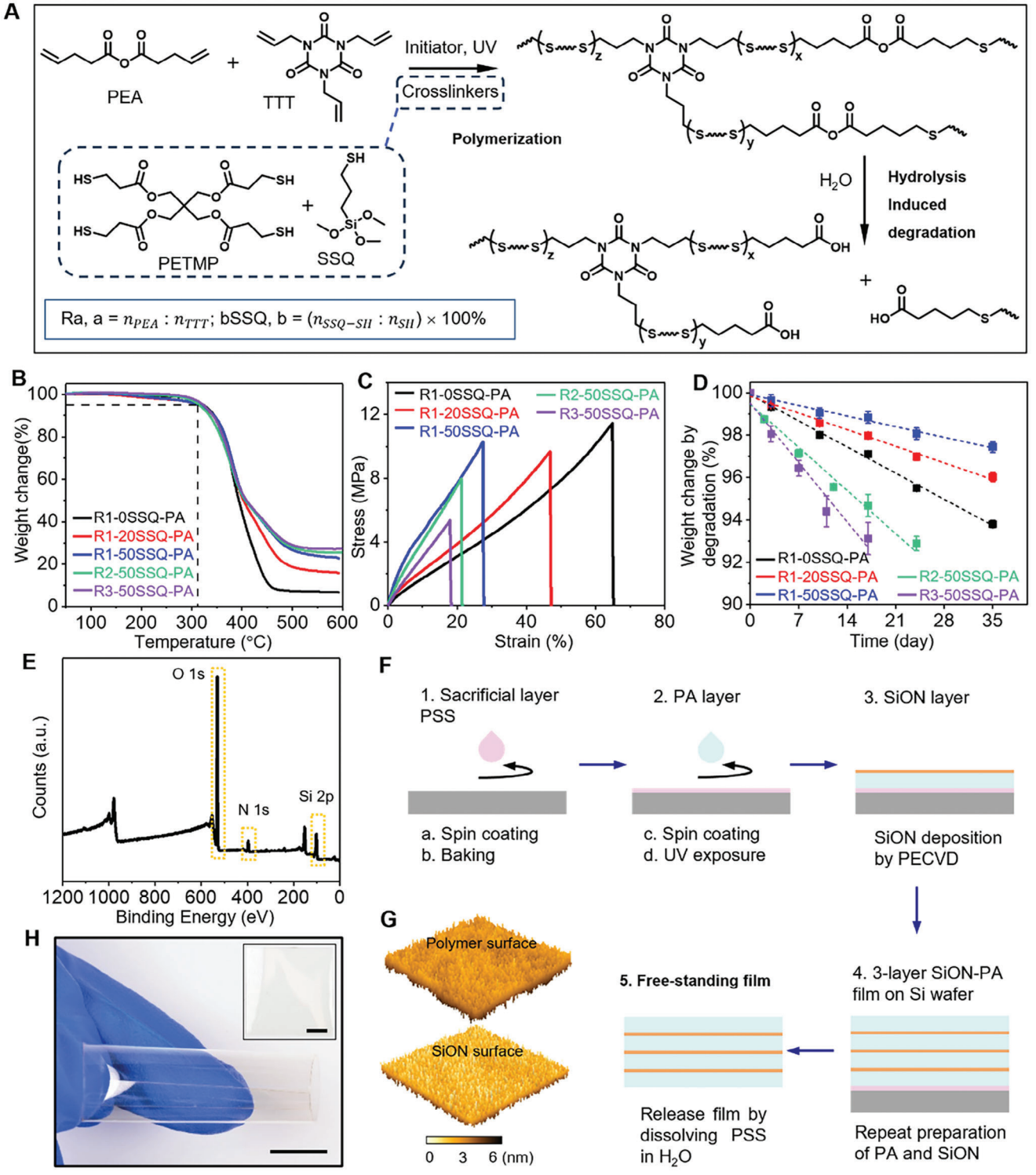

Figure 1. Preparation and characterization of polyanhydride (PA), silicon oxynitrides (SiON), and SiON-PA films. A) Illustration of the PA synthesis and hydrolysis-induced degradation pathway. B–D) Decomposition temperature (B), mechanical properties (C), and degradation behavior (D) of PA (thickness: 100 µm) with different compositions characterized by thermogravimetric analysis (TGA), dynamic mechanical analysis (DMA), and soak testing (three samples for each type of film), respectively. E) Elemental distribution of a SiON film grown via plasma-enhanced chemical vapor deposition (PECVD) characterized using X-ray photoelectron spectroscopy (XPS). F) Illustration of the process for preparing a free-standing 3-layer SiON-PA film. G) Surface roughness of PA and SiON characterized by atomic force microscopy (AFM, scanning size: 20 × 20 µm). H) Photographs of a 3-layer SiON-PA film. Scale bars: 1 cm.

and 6.79%, respectively (Figure 1E, Figure S6, and Table S1, Supporting Information).

Figure 1F illustrates the process for preparing a free-standing 3-layer SiON-PA film, where a layer of SiON-PA includes one layer of both SiON and PA. Cross-sectional scanning electron microscope (SEM) images of SiON-PA films enable precise visualization of the film structures, indicating strong interface adhesion between SiON and PA (Figure S7, Supporting Information). The total thicknesses of PA and SiON in these stacks are 100 and 2 μm, respectively, unless otherwise noted. A sacrificial layer of polystyrene sulfonate (PSS) dissolves in water to allow release from a silicon wafer substrate. Specifically, casting the PA monomer solution on a wafer coated with PSS followed by UV exposure and deposition of SiON via PECVD forms one layer of SiON-PA. Repeating the processes for forming films of PA and SiON yields multilayers of SiON-PA. Casting a final overlying layer of PA helps to suppress bowing of the released multilayer that otherwise occurs due to residual stresses in the SiON-PA, as shown in Figure S8 (Supporting Information). Atomic force microscope (AFM) images indicate that the PA and SiON sublayers have surface roughnesses around 1 nm (Figure 1G). The resulting multilayer SiON-PA films are flexible, mechanically robust, and transparent (≥90% with wavelength >500 nm),[30] as shown in Figure 1H and Figure S9 (Supporting Information). Results of finite element modeling and theoretical analysis reveal maximum strains in PA and SiON of 1-, 2-, 3-, and 4-layer SiON-PA films under different bending conditions (Figure S10A–D, Supporting Information, insets show architectures of SiON-PA films). The fracture strain of the SiON (≈1%) limits the minimum bending radii of multilayer SiON-PA films (number of film layers $m \geq 2$); the fracture strain of the PA (≈25%) determines that of 1-layer SiON-PA films. The strain distribution in a 3-layer SiON-PA film appears in Figure S10E (Supporting Information) as an example where the minimum bending radius is ≈2.4 mm. The minimum bending radius increases with the number of layers, as summarized in Figure S10F (Supporting Information).

2.2. Water Barrier Properties of Bioresorbable Multilayer SiON-PA Films

Studies of water barrier properties of multilayer SiON-PA films involve their use as encapsulants over patterned traces of Mg as a resistance test structure. A structure of PDMS forms a sealed reservoir for a solution of PBS applied on top of the multilayers with the Mg traces underneath, as illustrated in **Figure 2A** (see details in the Experimental Section). Reactions between Mg and water that permeate through the SiON-PA films lead to formation of magnesium hydroxide and associated dramatic changes in the optical and electrical properties of the traces. The water barrier properties of SiON-PA films can be described as the soaking time required to increase the resistance of the Mg test structure by 20% at 37 °C (Figure S11, Supporting Information). The average lifetimes are 49 ± 2, 54 ± 2, and 57 ± 1 days for 2-, 3-, and 4-layer SiON-PA films, respectively, when the molar ratio of PEA:TTT = 1 and molar ratio percentage of SSQ-SH = 50% (Figure 2B and Figure S11, Supporting Information, R1-50SSQ). The lifetimes for 1-layer SiON-PA films and bare PA films (Figure S12, Supporting Information) are 14 ± 2 days and 2.3 ± 0.3 h, respectively. The results demonstrate that 1) multilayer SiON-PA films (m = 2, 3, 4) have water barrier properties superior to those of 1-layer SiON-PA films and bare PA films; 2) increasing the number of layers (m = 2, 3, 4) of the SiON-PA films slightly improves the lifetime. Decreasing the amount of SSQ (Figure 2B, R1-20SSQ, R1-0SSQ) or increasing the amount of anhydride (Figure S13, Supporting Information, R2-50SSQ and R3-50SSQ) in the PA decreases the lifetimes. These results indicate that the chemical composition of PA affects the water barrier properties of SiON-PA films, which is likely due to reductions in the modulus and increases in the swelling of PA. The following experiments use the optimized composition of PA, R1-50SSQ. Additionally, given the practical consideration that adding a SiON-PA layer requires at least another 30 min in film fabrication, the 3-layer SiON-PA film serves as a representative multilayer structure to showcase the materials design strategy in the following experiments, unless otherwise noted.

Additional insights into the mechanisms of permeation follow from tests that involve arrays of Mg dots (100 × 100 arrays, each dot: 20 × 20 μm) sealed by 3-layer SiON-PA films (3L-R1-50SSQ) and immersed in PBS at 50 °C, in setups otherwise similar to those in Figure 2A. Grayscale analysis of images collected at various times appears in Figure 2C. The percentage of dark areas (corresponding to Mg dots) remains relatively constant during the first 11 days, then slightly decreases, and finally dramatically decreases after 20 days. Representative images in Figure 2D show that permeation at the locations of several dots occurs in 20 days and then spreads quickly afterwards. Similar phenomena occur with comparatively large, isolated Mg disks (diameter: 4 mm), for cases of encapsulation with 3-layer SiON-PA films (Figures S14 and S15, Supporting Information), 1-layer SiON-PA films (1L-R1-50SSQ, Figure S14, Supporting Information), and bare PA films (Figure S16, Supporting Information), in PBS and Dulbecco's Modified Eagle Medium (DMEM, a cell culture medium) at 50 °C. Mg disks sealed by 3-layer SiON-PA films display visible change in 20 days and those by 1-layer SiON-PA films and bare PA films in 2 days and 15–80 min, respectively. These observations suggest that water passes mainly through local defects, and that the multilayer structure effectively impedes this process.

2.3. Water Permeation Characteristics Through Bioresorbable Multilayer SiON-PA Films

Electrochemical approaches serve as a basis for monitoring the water permeation process through measurements of current leakage upon application of a voltage across a film and through electrochemical impedance spectroscopy (EIS). **Figure 3A** illustrates the setup, which involves a working electrode (WE: Au), a counter electrode (CE: Pt wire), and reference electrode (RE: Ag/AgCl) in an electrolyte bath (PBS, pH = 7.4, 10×10^{-3} M). Current leakage tests are similar but use only two electrodes (Au and Pt wire, Figure S17, Supporting Information). The films under test exist as coatings on a silicon wafer coated with Au (WE, thickness: 100 nm), sealed on top with a PDMS well to define the testing area (9 × 9 mm or 11 mm in diameter) and a reservoir

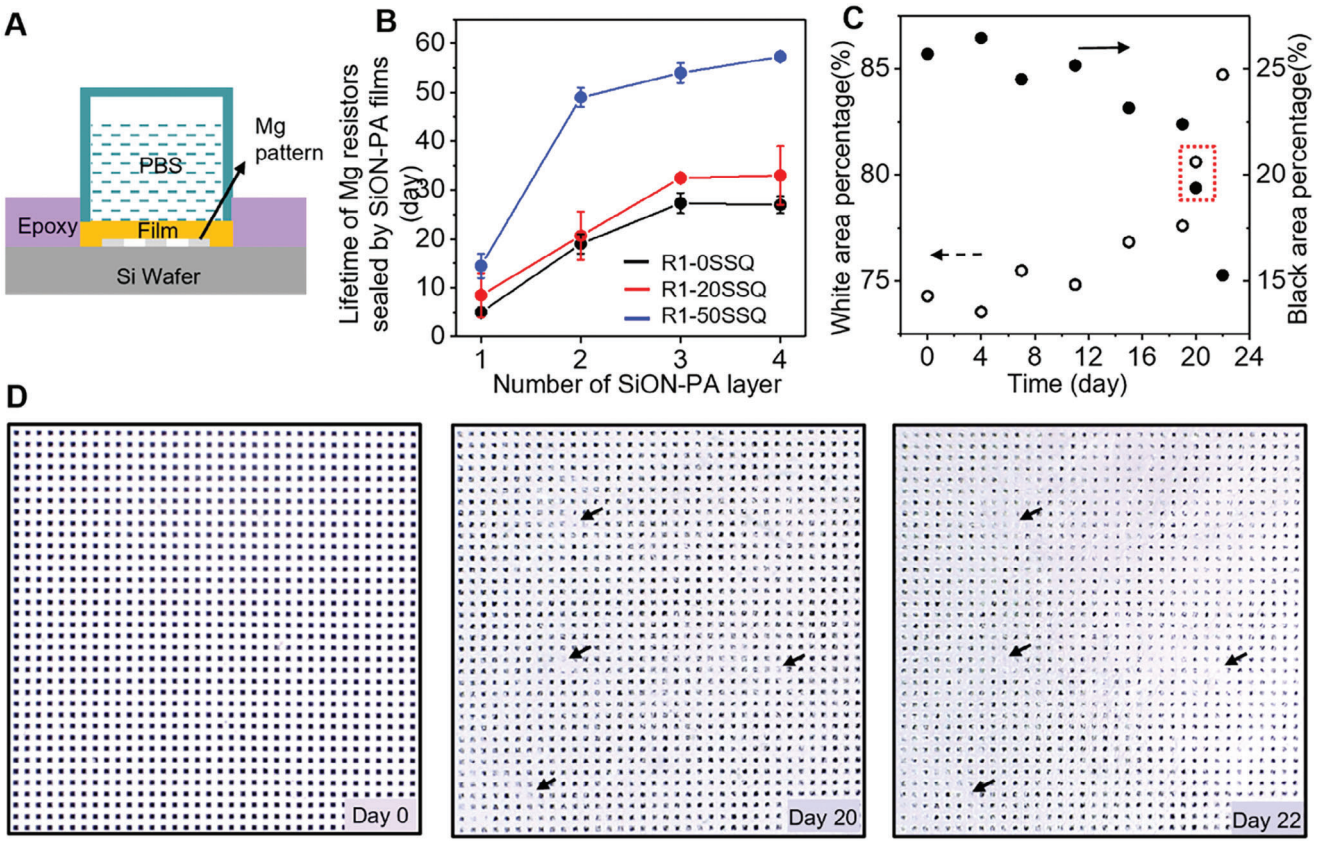

Figure 2. Water barrier properties of bioresorbable SiON-PA films. A) Experimental setup for evaluation of water barrier properties using Mg resistors and Mg dot arrays. B) The lifetime of Mg resistors sealed by SiON-PA films (time of Mg resistance increases by 20% in PBS (pH = 7.4, 10×10^{-3} M) at 37 °C, Figure S11) for different PA compositions (amount of SSQ) and numbers of SiON-PA layers (n = 1, 2, 3, 4). Evaluations for each type of film include at least two samples. C) Grayscale analysis of images of Mg dot arrays. Mg dot arrays are encapsulated with 3-layer SiON-PA films (3L-R1-50SSQ, soaked in PBS at 50 °C). D) Representative images of Mg dot arrays (dot: 20 × 20 μm; thickness, 100 nm) in (C). Arrows indicate the corrosion of Mg dots at day 20 due to water permeation across the film, spreading to a larger area at day 22 (Image size: 1.5 × 1.5 mm).

for the electrolyte. A constant potential of 3 V and a voltage with amplitude of 10 mV applied between the WE and CE enable measurements of current leakage and impedance (frequency range: 1 Hz – 100 kHz), respectively. A decrease in EIS phase in the low frequency range indicates the existence of defects in a film. A decrease in impedance with time follows from permeation of PBS into the films. The appearance of current leakage corresponds to permeation through the films.

EIS and leakage measurements suggest open defects in the SiON films (Figure 3B) and no open defects in the PA films but fast fluid permeation across their full area (<12 h, PBS at 50 °C, Figure 3C). By contrast, for 3-layer SiON-PA films, leakage appears after 20 days of immersion in PBS at 50 °C as the impedance decreases gradually (Figure 3D and Figure S18A, Supporting Information). For 1-layer SiON-PA films with the same total thickness, leakage appears after 1 day under the same condition, with decreasing impedance (Figure 3E and Figure S18B, Supporting Information). These results confirm that water permeates through films via local defects and that 3-layer SiON-PA SiON-PA films block water permeation more effectively than 1-layer SiON-PA films, consistent with observations from experiments with the Mg dot arrays and disks.

Additionally, compared with 1-layer SiON-PA films, when decreasing the total thickness of SiON-PA films while increasing the number of layers, for example two bilayers of 25-μm PA and 667-nm SiON, the time for water permeation increases from 1 day to 7 days (Figure S19, Supporting Information). These results highlight the key role of the multilayer structure in blocking water permeation, in some ways more important than the overall thickness. EIS and current leakage measurements indicate that water permeation times are nearly the same regardless of the thickness of an individual PA layer in 3-layer SiON-PA films (25 μm, Figure 3D and Figure S18A (Supporting Information), versus 15 μm, Figure 3F and Figure S18C, Supporting Information). This also indicates that PA has a negligible effect on directly blocking water permeation. Defect-rich multilayer SiON-PA films are good water barriers likely because the multilayer structure 1) leads to misalignment between uncorrelated defects in the various SiON layers and thus to tortuous pathways for water permeation, and 2) creates interfaces in adjacent SiON layers that reduce water concentration (or water flux) in the bottom layer of the multilayer SiON-PA films, as illustrated in Figure S20 (Supporting Information, additional studies see Note S1, Supporting Information). Some nondegradable barrier layers utilizing this multilayer strategy also present similar effects.[31–33]

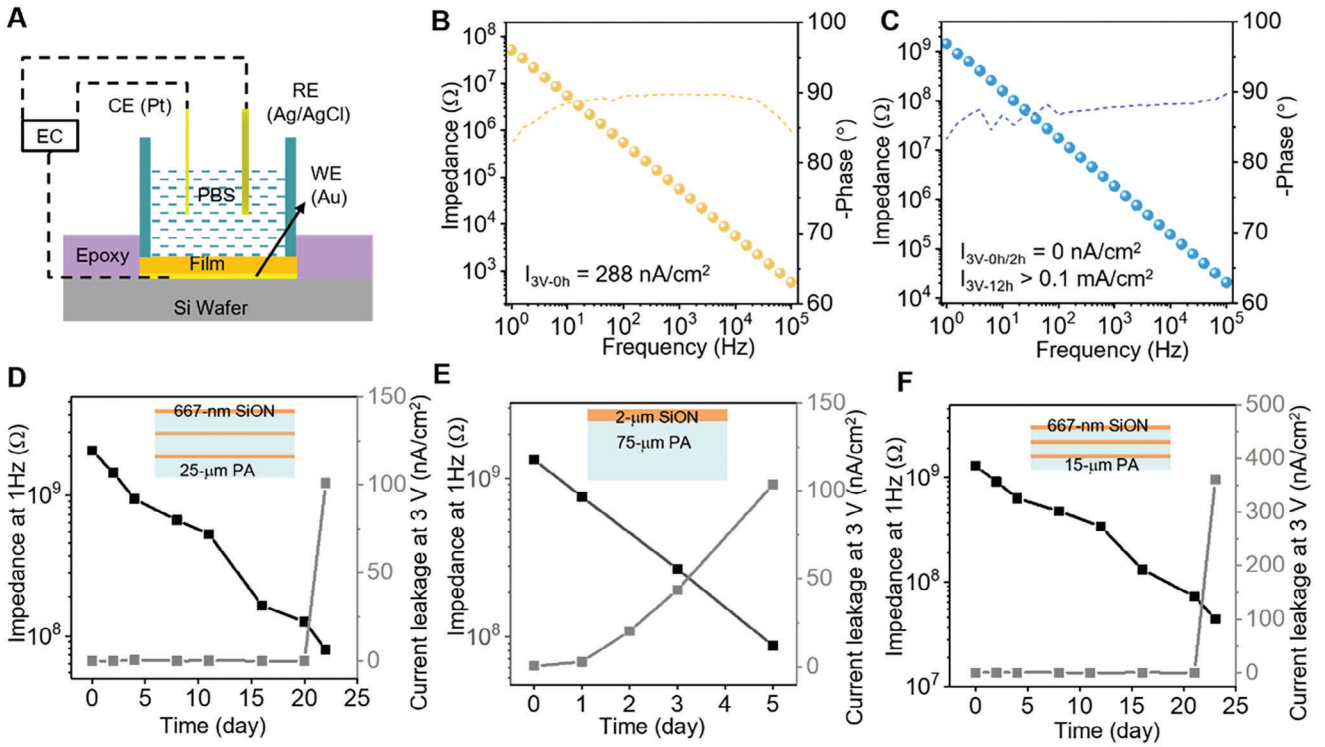

Figure 3. Electrochemical measurements on PA, SiON, and SiON-PA films. A) Experimental setup for impedance spectroscopy (EIS) measurements using a three-electrode system, including reference electrode (RE, Ag/AgCl), counter electrode (CE, Pt wire), and working electrode (WE, Au). B) Bode plot of a 2-μm SiON film. A current of 288 nA cm^{-2} appears when a voltage of 3 V is applied between Pt electrode and Au electrode. C) Bode plot of a 75-μm PA film. A large current (>0.1 mA cm^{-2}) appears after PA film is soaked in PBS for 12 h, indicating that water permeates fast through the entire PA film. D) Impedance at 1 Hz and current leakage of 3-layer SiON-PA films (three bilayers of 25-μm PA and 667-nm SiON). E) Impedance at 1 Hz and current leakage of 1-layer SiON-PA films (one bilayer of 75-μm PA and 2-μm SiON). F) Impedance at 1 Hz and current leakage of 3-layer SiON-PA films with PA sublayers having a reduced thickness (three bilayers of 15-μm PA and 667-nm SiON). Insets are illustrations of film architectures. PA here refers to R1-50SSQ. All films were soaked in PBS (pH = 7.4, 10×10^{-3} M) at 50 °C.

2.4. Theoretical Modeling of Reactive Diffusion for Water Permeation Across Multilayer SiON-PA Films

Theoretical modeling of reactive diffusion in these systems provides quantitative insights into the essential behaviors (**Figure 4**). A single-layer model applied to experimental studies of films of SiON (Figure S21, Supporting Information) yields the water diffusivity in the SiON, $D_{SiON} = 10^{-13.6}$ cm^2 s^{-1}, and the reaction rate constant for hydrolysis, $k_{SiON} = 10^{8.1\text{-}4530/T}$ s^{-1}, where T is the absolute temperature. Since the predicted hydrolysis rate of SiON is only ≈7.5 nm day^{-1} in PBS at 37 °C, and k_{SiON} has few effects on the modeling of the change in the resistance of the Mg test structures (Figure S22A, Supporting Information, simulation of resistance of Mg resistors sealed by 1-layer SiON-PA films), this reaction can be neglected at physiological temperature in studies of water permeation. Additionally, based on observed changes in resistance (Figure 2B and Figure S12, Supporting Information) and on current leakage and EIS measurements (Figure 3D,F), the PA has a negligible direct effect on blocking water permeation. The modeling thus considers that the SiON limits water permeation through the multilayer structure and that changes in resistance follow from both reaction and diffusion of water in the Mg. The model includes two types of interfaces: the SiON–SiON interface and the film–Mg interface (Figure 4A).

The time-dependent percentage change in resistance of the Mg test structure, $\Delta R = (h_0/h - 1) \times 100\%$, depends on the initial thickness h_0 and remaining thickness h, as obtained in the same manner as in the single-layer model (see Experimental Section). The film–Mg contact transfer coefficient (defined in Experimental Section),[34,35] $H_{film\text{-}Mg} = (2.0 \pm 0.3) \times 10^{-11}$ cm s^{-1}, follows from experimentally measured changes in the resistance of Mg structures protected by 1-layer SiON-PA films in PBS at 37 °C (Figure 4B). The SiON–SiON contact transfer coefficient,[34,35] $H_{SiON\text{-}SiON} = (3.0 \pm 0.2) \times 10^{-11}$ cm s^{-1}, follows from similar measurements of resistance but protected by 3-layer SiON-PA films (Figure 4C). With these parameters, the water concentration in 1-layer (Figure 4D) and 3-layer (Figure 4E) SiON-PA films after soaking in PBS at 37 °C for 10, 30, and 60 days, can be calculated. The water barrier effects at the SiON-SiON interfaces lead to abrupt decreases in concentration at those locations. For example, in the 3-layer SiON-PA films, the water concentration at the film–Mg interface is nearly zero even after immersion in PBS for 10 days at 37 °C, followed by a slow increase with time as expected. The cases of 2-layer (Figure S22B, Supporting Information) and 4-layer (Figure S22C, Supporting Information) SiON-PA films show similar results. Based on the water concentration at the film–Mg interface, the resistance changes of Mg traces sealed by 2-layer and 4-layer SiON-PA films can be

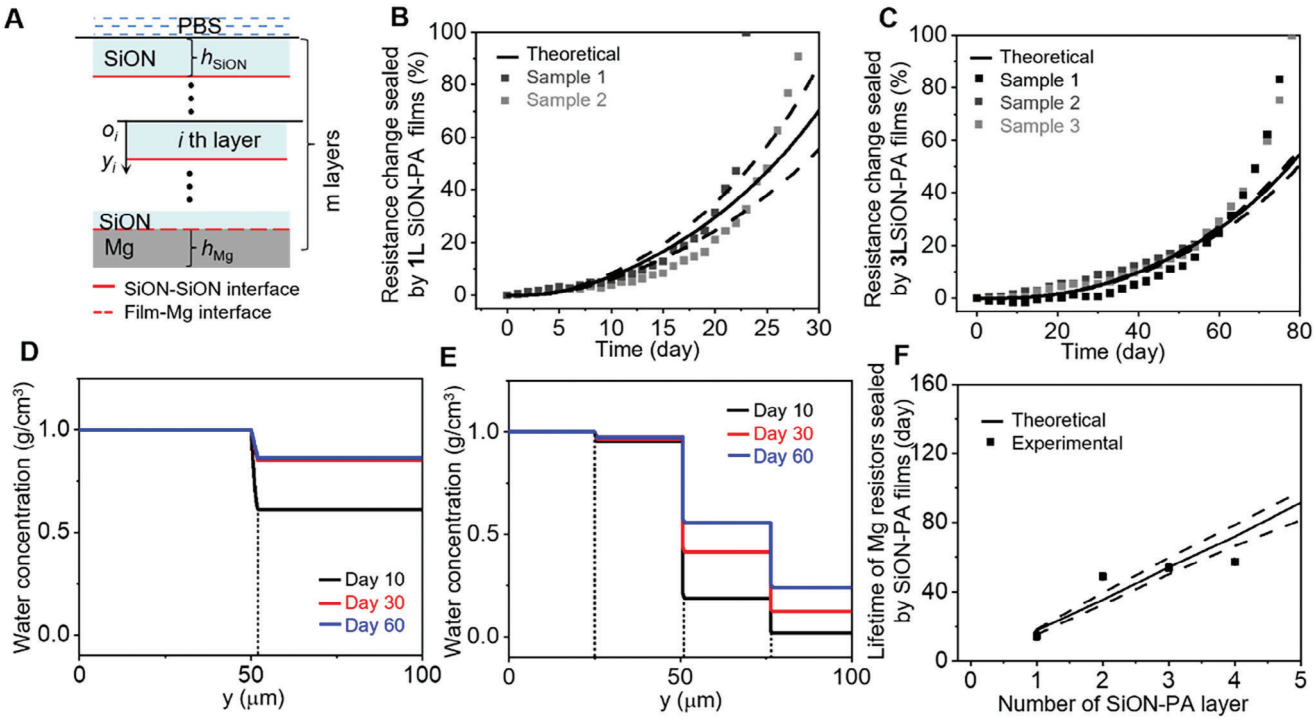

Figure 4. Theoretical modeling of reactive diffusion for water permeation across multilayer SiON-PA films. A) Illustration of a multilayer model for resistance changes of Mg resistors sealed by SiON-PA films. PA serves as an interface material between two adjacent SiON layers forming SiON-SiON interfaces. Another interface exists between the SiON-PA film and an Mg resistor, i.e., film–Mg interface. B) Theoretical and experimental resistance changes with time of Mg resistors sealed by 1-layer SiON-PA films. C) Theoretical and experimental resistance changes with time of Mg resistors sealed by 3-layer SiON-PA films. D) Water concentration distribution in a 1-layer SiON-PA film after 10, 30, and 60 days. E) Water concentration distribution in a 3-layer SiON-PA film after 10, 30, and 60 days. F) Theoretical and experimental water barrier properties of SiON-PA films with the number of SiON-PA layer (total thickness of SiON and PA: 2 and 100 μm, respectively). Water barrier properties are evaluated by the lifetimes of Mg resistors whose resistances increase by 20%. Dashed lines in B, C, and F indicate a deviation from the solid lines due to the errors in determining the contact transfer coefficient of film–Mg interface and dots are experimental data (PBS, pH = 7.4, 10×10^{-3} M, at 37 °C). PA here refers to R1-50SSQ.

determined, as summarized in Figure S22D,E (Supporting Information), respectively. The computed barrier properties, defined by the time for the resistance to increase by 20% in PBS at 37 °C, improve with the number of SiON-PA layers, consistent with the experimental results ($m \leq 4$, Figure 4F). A discrepancy occurs, however, when the number of film layers is greatly increased for a fixed total thickness of polymer and SiON. The cause may follow from increases in the densities of defects in the SiON layers as their thicknesses decrease, whereas the modeling assumes a constant density. Experimental support is in increases in current leakage with decreasing SiON thickness (Figure S23, Supporting Information). The increase is pronounced for thicknesses less than 1 μm, corresponding to the number of film layers $m > 2$. This phenomenon likely also explains the significant improvement in barrier properties of 2-layer SiON-PA films over those of 1-layer SiON-PA films, and the incremental additional improvements for three and four layers.

2.5. Biocompatibility of Bioresorbable Multilayer SiON-PA Films

In vitro and in vivo studies yield insights into the biocompatibility of these films (**Figure 5**). Testing involves samples of 3-layer SiON-PA films (3L-R1-50SSQ, 3L-R2-50SSQ) and related polymer films (R1-50SSQ-PA and R2-50SSQ-PA) with diameters of 5 mm and thicknesses of ≈100 μm, incubated in cell culture media in a 24-well plate for 2 days and then cultured with mouse fibroblast (L929) cells at 37 °C for another 3 days.[36] The results indicate no significant differences in the percentages of live cells with and without the films, suggesting that these materials and the products of their degradation are not harmful to mice fibroblast cells (Figure 5A,B, and Figure S24, Supporting Information).

In vivo results follow from implanting the 3-layer SiON-PA films (5 × 10 mm) in the dorsal subcutaneous region of mouse models for 4 and 8 weeks. Changes in the weights of the mice in the implanted and control groups at 4 and 8 weeks are nearly identical (Figure 5C). Figure 5D,E shows the weights of key organs, including heart, spleen, kidney, brain, lung, and liver, explanted at 4 and 8 weeks after implantation, and the distribution of Si in these organs measured by inductively coupled plasma optical emission spectrometry, respectively. These data also show minimum differences. Complete blood counts (CBC) and blood chemistry serve as additional indicators for organ-related responses. CBC reveals the average level of red blood cells, hemoglobin, hematocrit, platelets, and white blood cells (Figure 5F). Analysis of blood chemistry includes the level of

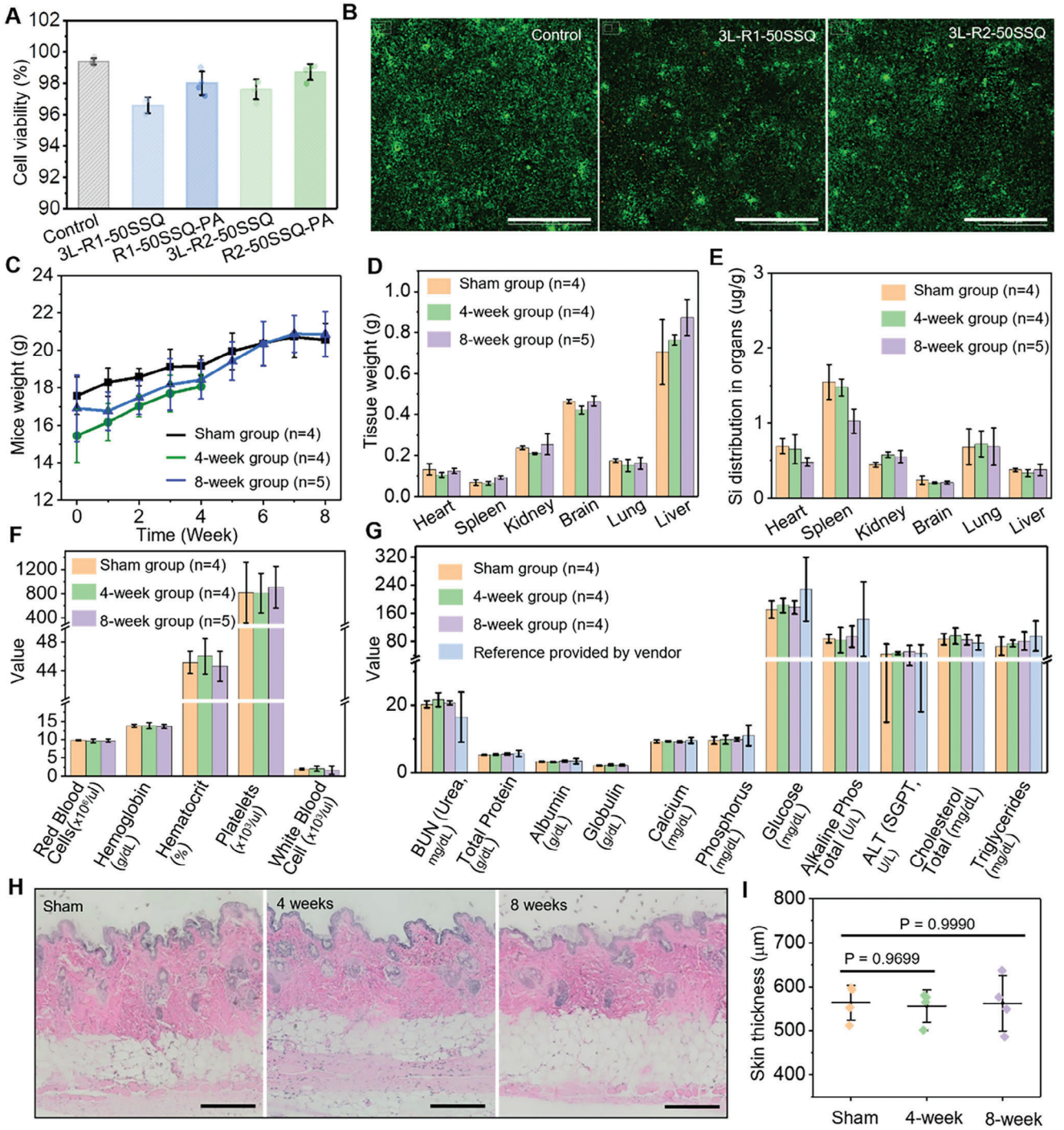

Figure 5. In vitro and in vivo studies on biocompatibility and biodegradation of3-layer SiON-PA films. A) Cell viability of 3-layer SiON-PA films (3L-R1-50SSQ, 3L-R2-50SSQ; R1 and R2 refer to the molar ratio of PEA/TTT = 1 and 2 respectively), and the related PA films (R1-50SSQ-PA and R2-50SSQ-PA). B) Fluorescence images of cells cultured with 3-layer SiON-PA films in contrast to a control assay. C) Weight change of mice with/without film implantation. Nine mice were implanted with 3-layer SiON-PA films: 4 mice in the 4-week group and five mice in the 8-week group. Four mice without film implantation were the sham group. (Film thickness: 100 μm; size: 5 × 10 mm). D) Tissue weight change of mice, including heart, spleen, kidney, brain, lung, and liver, in three groups. E) Silicon distribution in heart, spleen, kidney, brain, lung, and liver, in three groups of mice. F) Complete blood count (CBC) analysis from mice. G) Blood chemistry analysis on mice. H) Histological analysis on mice skin with/without film implantation. I) Average skin thickness of mice with/without film implantation. No significant differences exist among groups of Sham, 4-week, and 8-week analyzed using an ordinary one-way ANOVA with post hoc Tukey's means comparisons. Results in Figure 5C–G are presented as mean ± standard deviation. Scale bars: b. 1 mm; h. 200 μm.

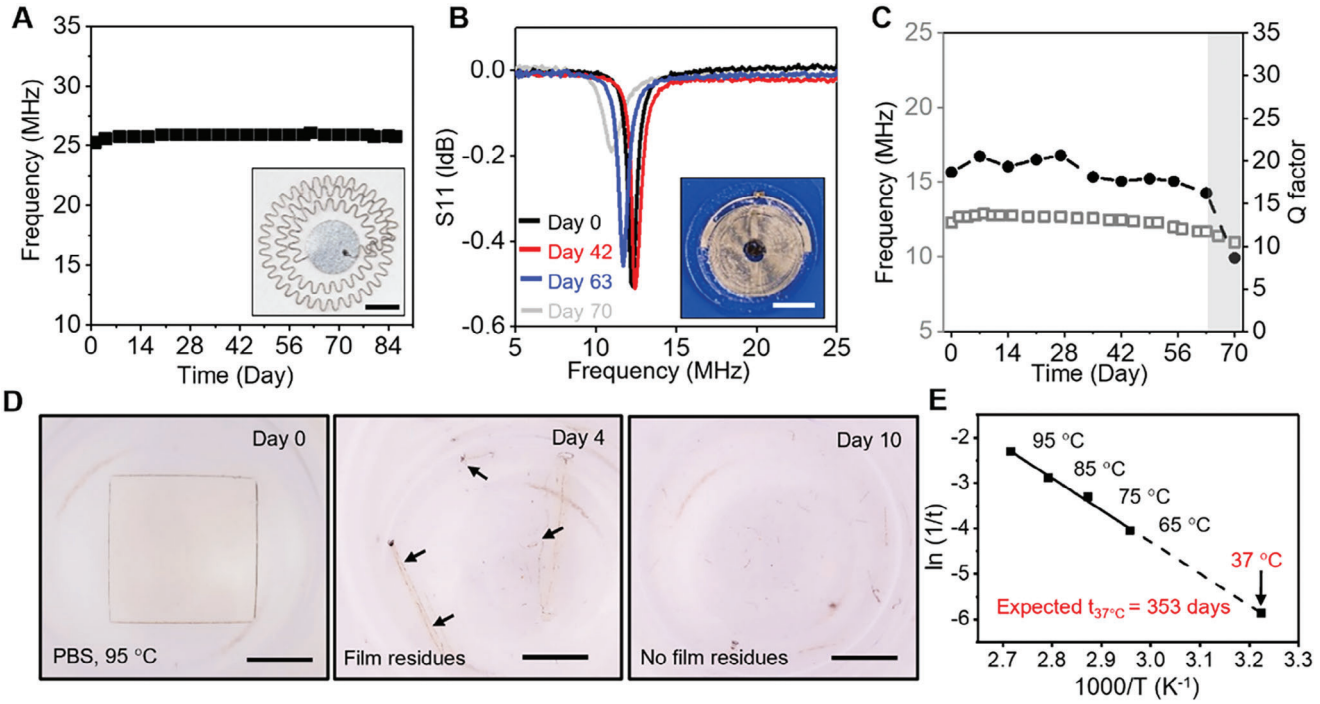

Figure 6. Device demonstrations of 3-layer SiON-PA films as encapsulating structures and studies of their degradation. A) Frequency stability of an LC circuit sealed on a glass slide by 3-layer SiON-PA films and soaked in PBS (pH = 7.4, 10×10^{-3} M) at 37 °C. Inset is a photo of the LC circuit. B) Radio frequency (RF) behavior of a power receiving modulus for wireless power transfer sealed on a glass slide by 3-layer SiON-PA films and soaked in PBS at 37 °C. Inset is a photograph of the power receiving modulus with a LED indicator. C) Frequency change of the power receiving modulus in B. D) Degradation process of 3-layer SiON-PA films (3L-R2-50SSQ) in PBS at 95 °C. E) Arrhenius plot of $\ln(1/t)$ versus $1000/T$. This illustrates the temperature-dependent degradation of 3-layer SiON-PA films, which are expected to fully degrade in 353 days at physiological temperature. Scale bars: 5 mm.

blood urea nitrogen, proteins, liver enzymes, glucose, lipids, and important minerals etc. (Figure 5G). Both tests show no significant differences between the implanted and control groups. Histological analysis of the skin and muscles in the implantation region (Figure 5H,I, and Figure S25, Supporting Information), including skin morphology, skin thickness, morphology of muscle cells, and the average sizes of myofibers, also indicates negligible differences.

2.6. Device-Level Use of Multilayer SiON-PA Films as Encapsulating Layers

Inductor–capacitor (LC) circuits and systems for wireless power transfer serve important roles in many applications of bioresorbable medical devices, from temperature and pressure sensors,[37,38] to cardiac pacemakers,[10,12] to nerve stimulators.[2,11] A demonstration example reported here uses a bioresorbable LC circuit (metal: Zn; dielectric layer: PLGA) and a bioresorbable power receiving module (metal: Mo) to illustrate the use of multilayer SiON-PA films as water barriers. The experiments involve recording the radio frequency (RF) behavior using a vector network analyzer. **Figure 6A** shows the peak frequency of a LC circuit (inset figure) built on a glass substrate and encapsulated with a 3-layer SiON-PA film, immersed in PBS at 37 °C. The frequency remains unchanged for at least 12 weeks. Figure 6B presents the RF behavior of a wireless power receiving module, similarly encapsulated with a 3-layer SiON-PA film. The power transmission performance appears visually through a wirelessly activated light-emitting diode (LED). Here, a signal generator supplies RF power to a transmitter coil (60 mm diameter, 3 turns) placed over the receiving coil. The RF behavior changes by a negligible amount in 63 days (9 weeks) and the LED operates after immersion in PBS at 37 °C for at least 70 days. Quantitative analysis of the peak frequency and quality factor (Q factor) of the receiving coil, as important parameters that influence the power transfer efficiency, shows unchanged behavior for 9 weeks, followed by a shift of the peak frequency to lower values and a decrease in the Q factor (Figure 6C). By comparison, the RF behavior of an otherwise similar wireless power receiving module encapsulated with PLGA varies greatly, and the LED fails within a day.

Timescales for complete degradation following a stable operating period are also important. Figure 6D shows the evolution of 3-layer SiON-PA films (12 × 12 mm) immersed in PBS at 95 °C, indicating that the constituent materials disappear in 10 days. Results of similar experiments performed at different temperatures[39] are consistent with Arrhenius scaling, $\ln(1/t) = (-E_a/R)\ (1/T) + \ln A$, where t is the degradation time, T is the temperature, E_a is the activation energy for degradation reactions, A is the pre-exponential factor, and R is the universal gas constant. Extrapolations using this scaling suggest that these multilayer SiON-PA films fully degrade within 1 year (Figure 6E).

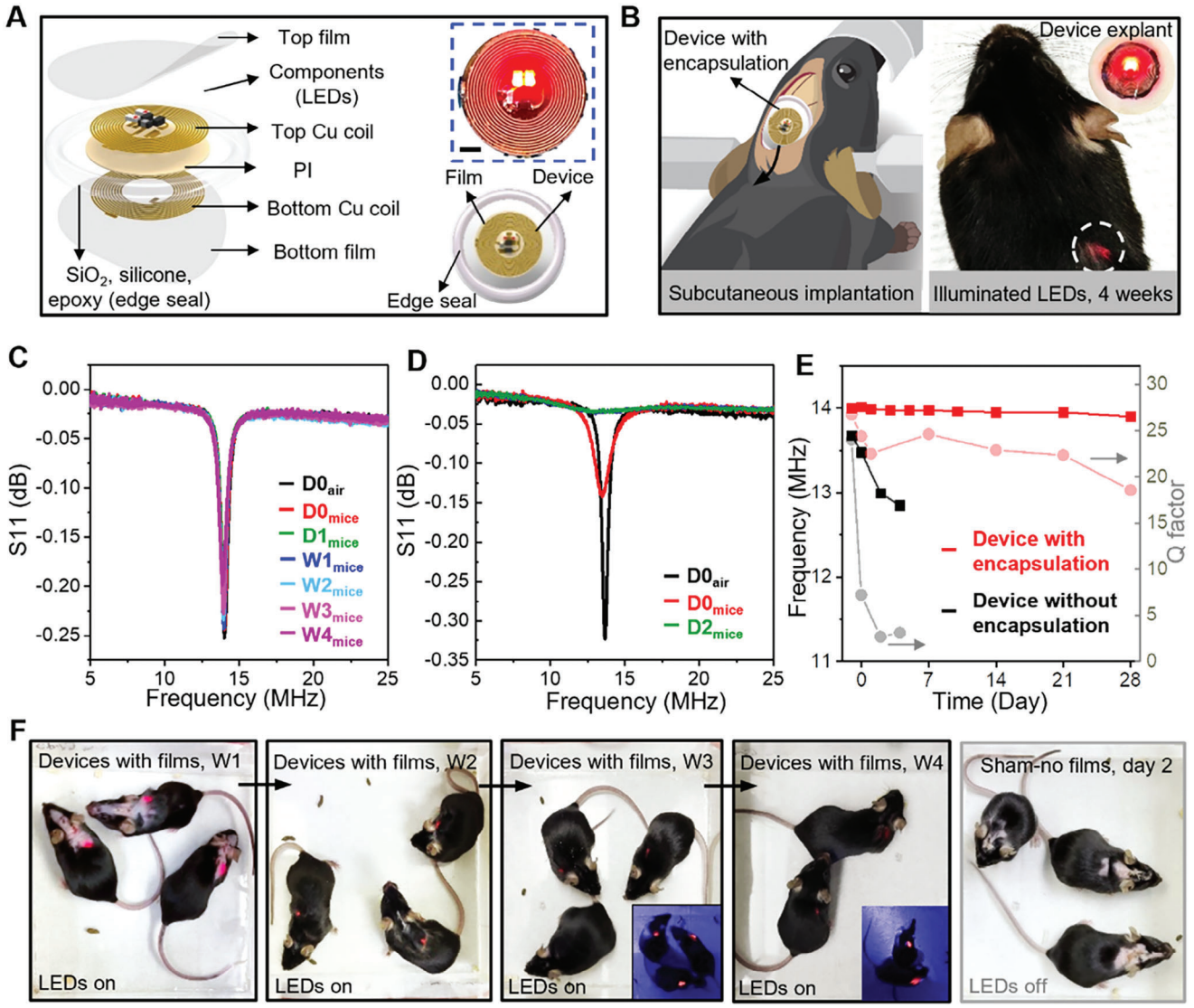

Figure 7. Optoelectronic device demonstration of water barrier performance of 3-layer SiON-PA films through implantation studies in mice. A) Exploded view schematic diagram of the device and its encapsulation. Inset shows activated LEDs, indicating proper functioning of the device. B) Schematic diagram of the subcutaneous implantation and photographs of LED activation upon implantation for 3 and 4 weeks. Inset is a photograph of a device explanted at the 3-week time point, showing wireless activation of the LEDs, and the optical transparency of the encapsulating films. C) RF behavior of devices encapsulated using 3-layer SiON-PA films. D) RF behavior of devices without encapsulation. E) Frequency and *Q* factor of devices, shown in C and D, changing with implantation time in mice. F) Photographs of mice implanted with devices during wireless activation. Devices with encapsulation using 3-layer SiON-PA films can be wirelessly powered after implantation in mice ($n = 3$) for 4 weeks, as evidenced by the activated LEDs. Those without encapsulation (sham group, $n = 3$) fail to function after implantation for 2 days. One mouse was sacrificed to harvest the device (B, inset) after 3 weeks. Insets show activation of the LEDs in a darkroom for improved visualization. Scale bar: 1 mm.

2.7. Device-Level Demonstration of Multilayer SiON-PA Films in Mice

Figure 7A presents an exploded view schematic diagram of the wireless optoelectronic device and its encapsulation using 3-layer SiON-PA films. The diameter of the device before and after encapsulation is 6 and 10 mm, respectively. Subcutaneously implanted devices in mice retain their functionality even after 4 weeks, as evidenced by the light emission from activated devices in Figure 7B and Figure S26 (Supporting Information). Inspection of a representative device explanted at the 3-week time-point, shows expected functionality and indicates that the SiON-PA films remain transparent, enabling the optoelectronic device to operate efficiently without compromising its optical performance in vivo. Figure 7C,D presents the RF characteristics of devices with and without encapsulation using 3-layer SiON-PA films, respectively. Figure 7E summarizes the changes in resonant frequencies and Q factor values of devices during the implantation period (4 weeks) in mice. Both parameters remain stable for the cases with encapsulation, whereas those without show significant decreases, caused by exposure to biofluids in mice. Figure 7F presents photographs of mice implanted with

optoelectronic devices with (n = 3) and without encapsulation (sham group, n = 3). Cases with encapsulation show expected function through LED illumination for more than 4 weeks. By contrast, devices without encapsulation rapidly fail to function, typically after 2 days. These results highlight the superior water barrier performance of SiON-PA multilayer films within mice. We note that encapsulation using wax with a thickness of 300 µm, can support operation of similar devices for 7 days postimplantation, as published previously.[2]

3. Conclusion

In conclusion, this work introduces an organic–inorganic multilayer design strategy for bioresorbable encapsulating structures that can protect implantable electronic devices from biofluids to ensure reliable operational performance over timeframes longer than those possible with previously reported materials approaches. Tailored schemes in polymer synthesis and chemical vapor deposition of films of PA and SiON, respectively, provide means for controlling the rates of degradation. The resulting multilayer SiON-PA films (total thickness of PA and SiON: 100 and 2 µm) can effectively block water transport for at least 7 weeks (49 ± 2, 54 ± 2, and 57.3 ± 0.6 days for 2-, 3-, and 4-layer of SiON-PA films, respectively). Comprehensive experimental and modeling studies demonstrate that the multilayer structure plays a significant role in water barrier properties due to formation of tortuous permeation paths and low water concentration in the bottom layers. Investigations of viability in cell cultures and in animal models indicate that the multilayer SiON-PA films have both good biocompatibility and superior water barrier performance. Successful demonstrations as encapsulating structures for LC circuits, wireless power transfer systems, and wireless optoelectronic devices suggest that the materials strategy introduced here may find broad and immediate applications for a range of practical electronic devices that are capable of resorption in biological and environmental settings.

4. Experimental Section

Polymer Synthesis and Characterization: Synthesis of the polyanhydride polymers, referred to as Ra-bSSQ-PA, where a is the molar ratio of PEA to TTT and b is the molar percentage of the thiol group from SSQ, relied on UV initiated thiol-ene reactions. The synthesis process began with mixing two cross-linkers, (3-mercaptopropyl)trimethoxysilane (0.05 mol, 9.8 g, Sigma-Aldrich) and diluted hydrochloric acid (0.15 mol, 2.7 g; 0.2 M, 37% HCl, Sigma-Aldrich) added to a 40-mL glass vial while stirring for 30 min. Pentaerythriol tetrakis(3-mercaptopropionate) (PETMP, 0.0125 mol, 6.1 g, Sigma-Alderich) was then added while stirring for 24 h. The hydrolysis and condensation of silane formed silsesquioxane (SSQ, b = 50). The next step removed the volatile reaction byproducts and water by vacuum drying the mixture of cross-linkers until the weight did not change, followed by adding two alkyne monomers, 4-pentenoic anhydride (PEA, 0.02 mol, 3.6 g, Sigma-Aldrich), and 1,3,5-triallyl-1,3,5-triazine-2,4,6(1H,3H,5H)-trione (TTT, 0.02 mol, 5.0 g, Sigma-Alderich). Adjusting the molar ratio of PEA and TTT (a = 1, 2, and 3) produced polymers with different degradation rates and swelling properties. Adding a photo initiator, 2,2-dimethoxy-2-phenylacetophenone (DMPA, 1 wt%, Sigma-Aldrich) or 2-hydroxy-4′-(2-hydroxyethoxy)−2-methylpropiophenone (Irgacure 2959, 1 wt%, Sigma-Aldrich), completed the preparation of the solution for the polymerization. The solution was then filtered using syringe filters (pore size: 0.2 µm, PTFE membrane; Thermo Fisher Scientific) and spin-cast onto a silicon wafer coated a thin layer of polystyrene sulfonate (PSS, thickness: 2 µm; filtered using syringe filters with pore size of 0.2 µm; Sigma-Aldrich) as a sacrificial layer to facilitate the release of polymer from the wafer. UV irradiation (365 nm, 65 mW cm^{-2}; UV curing machine F300, Inpro Technologies, Inc.) initiated the thiol-ene reaction. The spinning speed and time defined the thicknesses, measured using a stylus profilometer (Dektak-8, Veeco, USA).

FTIR measurements (Figure S1, Supporting Information) indicated that 97% of the thiol groups reacted with alkyne monomers within 120 s in the synthesis of a 100-µm polymer film. These results provided approximate times for UV irradiation of films with different thickness, for example, 150, 75, and 30 s for films with thicknesses of 100, 50, and 20-µm, respectively. To confirm the applicability of polymers in the growth of SiON via PECVD, the thermal properties, including decomposition temperature (Figure 1B), thermal transition temperature (Figure S3A, Supporting Information), and coefficient of thermal expansion (CTE, Figure S3B, Supporting Information), were characterized using TGA (DSC Q400, TA Instruments), DSC (DSC Q400, TA Instruments), and thermomechanical analysis (TMA Q400, TA Instruments), respectively. The mechanical properties (Figure 1C and Figure S4, Supporting Information), specifically the stress–strain responses, were characterized by DMA (RSA-G2 solids analyzer, TA Instruments). The optical transparency of the films was measured using a UV/Vis/NIR Spectrophotometer (Figure S9, Supporting Information; LAMBDA 1050, PerkinElmer). To test film swelling (Figure S5, Supporting Information) and degradation (Figure 1D), films were soaked in PBS at 37 °C and their wet and dry weights were measured using a microbalance (XPR2, Mettler Toledo). Film surface roughness and wettability were characterized by AFM (Figure 1G; Dimension Edge, Bruker) and contact angle measurements, respectively (Figure S2, Supporting Information, VCA Optima XE).

SiON Growth and Characterization: SiON films were deposited via PECVD at 180 °C (SiH_4 100 sccm, NH_3 300 sccm, N_2 400 sccm, and N_2O 1420 sccm; LPX CVD, SPTS Technologies Ltd., UK) at a high frequency (13.65 MHz), with thickness adjusted through the deposition time. The elemental percentages of the resulting films were characterized using XPS (Figure 1E, Figure S6, and Table S1 (Supporting Information); ESCALAB 250Xi, Thermo Fisher Scientific) after in situ etching of the films for 120–240 s.

Fabrication Process of Free-Standing SiON-PA Films: Fabrication involved casting a sacrificial layer of PSS on a silicon (Si) wafer, repeating the steps for preparation films of PA and SiON, and then releasing the resulting multilayers from the wafer by removing the PSS. Specifically, the process began with spin-coating a thin layer of PSS solution and baking at 110 °C for 30 s to form a film of PSS (thickness: 2 µm) on a wafer. Coating with a solution with monomers followed by exposure to UV formed a film of PA with thickness controlled by the spinning speed and time. PECVD defined a film of SiON with thickness determined by deposition time. Repeating this process followed by coating a final layer of PA on top completed the process. Release by soaking in water for a few hours yielded large-scale free-standing SiON-PA films. Rinsing with water and drying with N_2 followed by cutting using a CO_2 laser ablation system (VLS3.50, Universal Laser) yielded small pieces with desired shapes.

The overall thicknesses of SiON and PA in multilayer SiON-PA films were 2 and 100 µm, respectively, regardless of the number of film layers. One layer of SiON-PA film consisted of one single layer of SiON and one single layer of PA. Thus, the number of SiON-PA layers determined the thicknesses of one single layer of SiON and PA in the multilayer assembly. Free-standing SiON-PA films included an additional layer of PA on top. For example, a 3-layer SiON-PA film (Figure 1F) involved three bilayers of 25-µm PA and 667-nm SiON as well as a layer of 25-µm PA on top; a 1-layer SiON-PA film included one bilayer of 50-µm PA and 2-µm SiON as well as a layer of 50-µm PA on top.

Numerical Simulation and Theoretical Modeling for Minimum Bending Radii of Multilayer SiON-PA Films: Numerical simulation by the finite element method (FEM) and analytical modeling revealed mechanical aspects of the bendability of multilayer SiON-PA films. ABAQUS software simulated the distribution of strains in the PA and SiON of multilayer SiON-PA films with different bending radii (Figure S10, Supporting Information). A plane strain model with the element CPE8R, is consistent with film thick-

nesses (micron-scale) that are much smaller than the width and length of the films (centimeter-scale) 32.[40] A fine mesh (the mesh size: 1/200 of the length of the model) allowed for convergent numerical results with high accuracy. Imposing a rotation on two rigid bodies attached to both ends of the film simulated the bending process. The values of the Young's modulus and Poisson's ratio of SiON are 78 Gpa[41,42] and 0.23,[43] and those of PA are 56 MPa and 0.495,[44,45] respectively. The in-plane strain in a film is $\epsilon(\gamma) = (\gamma_{neutral} - \gamma)/\rho$ in a similar coordinate system to the single-layer model (Figure S21A, Note S1, Supporting Information). $\gamma_{neutral}$ refers to the location of the neutral mechanical plane, which is also the film mid-plane due to the structural symmetry with respect to the mid-plane, and ρ is the bending radius of the mid-plane. Accordingly, the maximum strain of a film is $\epsilon_{max} = d_{max}/\rho$, where d_{max} is the maximum distance from the mid-plane to the surface of the film. Figure S10A–D (Supporting Information) presents the theoretical maximum strains (lines) in SiON and PA layers of 1-, 2-, 3-, and 4-layer SiON-PA films under different bending radii. The results obtained by FEM (dots) are consistent with these calculations. Additionally, the minimum bending radius was determined by the fracture limit of SiON, ≈1.1%.[41] Figure S10E (Supporting Information) demonstrates the strain distribution in a 3-layer SiON-PA film for a bending radius of 2.43 mm, corresponding to the limiting strain in SiON. The dependence of the minimum bending radius on the number of film layers is summarized in Figure S10F (Supporting Information). The results indicated that the bendability of multilayer SiON-PA films, as opposed to the minimum bending radius, decreases with increasing number of film layers, as expected.

Evaluation of Water Barrier Properties Using Mg Resistors: Mg resistors were fabricated by photolithography and liftoff of Mg deposited by electron beam (e-beam) evaporation on glass slides or Si wafers. The fabrication process began with cleaning of the substrates using acetone, isopropanol, H_2O, and IPA in sequence and drying using a N_2 gun. Spin-coating a layer of photoresist (PR, AZ5214, MicroChemicals) on the cleaned substrates (3000 rpm for 30s), baking the PR (110 °C for 60 s), exposing it to UV in patterns corresponding to those of the Mg resistors (405 nm, dose 60 mJ cm^{-2}; MLA 150, Heidelberg Instruments, Germany), developing the PR to display the pattern (AZ917 for 40 s, MicroChemicals), rinsing with DI water, and drying with a N_2 gun. Mg resistor layouts were designed using AutoCAD and converted into a pixel image for UV exposure process. Mg deposition (deposition rate: 0.15—0.25 nm $^{-1}$s, total deposition thickness: 300 nm) occurred by e-beam (AJA International Inc., MA, USA). Rinsing the substrates after deposition using acetone lifted off the PR and the Mg in the undesired areas to leave patterned traces that defined the Mg resistors. To facilitate the resistance measurements, Cr/Au (10/100 nm) connecting pads were deposited through polyimide (PI, Goodfellow, USA) shadow masks via electron beam evaporation.

Measuring the resistances of such Mg resistors encapsulated by films under test and immersed in PBS yielded quantitative assessments of their water barrier properties. Application of these encapsulating films involved manual placement on top of the resistors with a small force to remove air pockets and ensure good contact. A polydimethylsiloxane (PDMS) tube positioned on top of the film, with the outer wall sealed using marine epoxy (1 919 324, Loctite), formed a containing structure to hold the PBS (pH = 7.4, 10×10^{-3} M). The setup was then stored in an oven (37 °C). The resistances were measured once per day at room temperature (22 °C) using a digital multimeter.

Water Permeation Assessed by Mg Dot Arrays and Disks: The fabrication and setup for experiments using Mg dot arrays and disks were similar to those for Mg resistors. An optical microscope (VHX-6000 Series, Keyence, Japan) was used to observe the time-dependent corrosion of Mg through the backside of the glass substrate. Accelerated testing involved placing the setup in an oven at 50 °C. The corroded areas, present as white in the images, were analyzed using gray scale analysis of ImageJ.

Electrochemical Measurements: Electrochemical measurements were performed using a three-electrode method, including a WE (Au), a RE (Ag/AgCl), and a CE (Pt wire), via a potentiostat/galvanostat instrument (Autolab Metrohm, Switzerland). A film under test was fabricated in situ on a silicon wafer with a surface coating of Cr (thickness: 10 nm) and Au (thickness: 100 nm) as the WE. A PDMS well (9 × 9 or 11 mm in diameter) sealed on top of the film using marine epoxy defined a testing area that was filled with PBS (pH = 7.4, 10×10^{-3} M) as the electrolyte. To monitor the current leakage, a constant potential (1 or 3 V) applied between the WE and CE. Measurements of impedance used a voltage of 10 mV applied between the WE and CE with the CE and RE immersed in PBS. The measurement frequency ranged from 1 Hz to 100 kHz. A decrease in impedance follows from permeation of PBS into the films. The appearance of current leakage corresponds to permeation through the entire thickness.

Theoretical Solution of the Reactive Diffusion Models: Single-Layer Model: A one-dimensional model is appropriate (Figure S21, Supporting Information) because the total thickness (in micrometer scale) of the films is much smaller compared to their widths and lengths (both in centimeter scale. The water diffusivity in SiON, D_{SiON}, and its reaction rate constant with SiON, k_{SiON}, are important parameters. The governing reactive diffusion equation is $D_{SiON}\partial^2 w/\partial\gamma^2 - k_{SiON}w = \partial w/\partial t$ ($0 \le \gamma \le h_{SiON}$), where h_{SiON} is the initial thickness of SiON and w is water concentration, depending on both location γ and time t. A constant water concentration, $w_0 = 1$ g cm^{-3}, at the top surface of SiON, and a water-proof substrate at the bottom surface of SiON correspond to boundary conditions $w|_{\gamma=0} = w_0$ and $\partial w/\partial\gamma|_{\gamma=hSiON} = 0$, with the latter indicating a zero-water flux condition. The water concentration in SiON is zero in the initial state, $w|_{t=0} = 0$ ($0 \le \gamma \le h_{SiON}$). The finite integral transform and Laplace transform methods are applied to give a theoretical solution of w (see Note S2[46], Supporting Information, for details). The thickness of material dissolved, $h_{dissolved}$, is obtained by the integration of $h_0 kwM/(q\rho M_{H2O})$ over both γ and t, and the time-dependent thickness change, h, is obtained by $h = h_0 - h_{dissolved}$. Here, q is the number of water molecules that react with each molecule of a material, ρ the mass density, and M and M_{H2O} the molar masses of the material and water, respectively. For SiON in this study, $M_{H2O} = 18$ g mol^{-1}, $\rho_{SiON} = 2.344$ g cm^{-3} (Table S2, Supporting Information), $M_{SiON} = 1958$ g mol^{-1}, and $q_{SiON} = 72.5$ according to the degradation equation, $4\ Si_{31}O_{62}N_7 + 290\ H_2O \rightarrow 124\ Si(OH)_4 + 28\ NH_3 + 21\ O_2$.

Multilayer Model: The final governing equations for an m-layer film and one layer of Mg are $D_i\partial^2 w^i/\partial\gamma_i^2 - k_i w^i = \partial w^i/\partial t$ ($0 \le \gamma_i \le h_i$) (i = 1, 2, 3, ..., m+1), where h_i is the thickness of the i th layer and γ_i indicates the local coordinate system for the i th layer. Here, $D_i = D_{SiON}$ and $k_i = 0$ for i = 1, 2, 3, ..., m; $D_{m+1} = D_{Mg}$ and $k_{m+1} = k_{Mg}$. The boundary conditions at the top and bottom surfaces of the multilayer film in the model correspond to a constant water concentration, $w_0 = 1$ g cm^{-3}, and zero water flux, respectively. Combined with the continuity condition of water flux at the interface between the i th and i+1 th layers (i = 1, 2, 3, ..., m), $D_i\partial w^i/\partial\gamma_i|_{\gamma i = hi} = D_{i+1}\partial w^{i+1}/\partial\gamma_{i+1}|_{\gamma i+1=0}$, an interfacial jump condition is applied[34,35]: $D_i\partial w^i/\partial\gamma_i|_{\gamma i = hi} = H_i(w^{i+1}|_{\gamma i+1=0} - w^i|_{\gamma i = hi})$, which reveals a flux-dependent water concentration difference across the interface, where H_i is the interfacial contact transfer coefficient. The finite integral transform and Laplace transform methods are applied to give a theoretical solution of w (see Note S1, Supporting Information, for details). Additionally, for the dissolution of Mg, $k_{Mg} = 1.2 \times 10^{-3}$ s^{-1}, $D_{Mg} = 6.0 \times 10^{-12}$ cm^2 s^{-1},[47] $\rho_{Mg} = 1.738$ g cm^{-3}, $M_{Mg} = 24$ g mol^{-1}, and $q_{Mg} = 2$ according to the dissolution reaction $Mg + 2H_2O \rightarrow Mg(OH)_2 + H_2$.

Biocompatibility and Biodegradation In Vitro: A mouse fibroblast cell line (L-929 P6 cells, ATCC CCL-1) was used for the in vitro cytotoxicity and biocompatibility tests. The culture media included Gibco DMEM (Thermo Fisher Scientific), 10 vol% fetal bovine serum (FBS, 10 vol%, Thermo Fisher Scientific), and penicillin-streptomycin (1 vol%, Thermo Fisher Scientific). The films under test (diameter: 5 mm, thickness: 100 µm) were first sterilized using a steam sterilizer for 25 min at 121 °C (or UV irradiation overnight) and then added to the culture media in a 24 well plate for 2 days prior to testing with L929 cells. The materials consisted of 3-layer SiON-PA films with different polymer compositions (3L-R1-50SSQ and 3L-R2-50SSQ) and the associated PA films (R1-50SSQ-PA and R2-50SSQ-PA). L929 cells were seeded in 24-well plates and cultured with these films and the conditioned medium at 37 °C with 5% CO_2 for another 3 days separately, where the films floated on the surface of the culture medium. The cells cultured with media only were control groups. Each group had four wells. The cell viability was tested using an Invitrogen Live/Dead cytotoxicity kit (L3224, Thermo Fisher Scientific). Specifically, calcein AM (5 µL) and ethidium homodimer-1 (20 µL) were added

to Dulbecco's PBS (DPBS, 10 mL, Thermo Fisher Scientific) to prepare a staining solution. After removing the medium and the films from the cells, the staining solution (400 µL) was added to each well and incubated 30 min at room temperature, followed by replacing the staining solution with 0.5 mL DPBS each well. The stained cells were then ready for imaging using a confocal microscope (SP8, Leica). Calcein generated from calcein-AM by esterase in the live cells exhibits strong green-fluorescence (excitation/emission ≈490/515 nm), while ethidium homodimer-1 binds to the DNA double helix of dead cell membranes and emits red fluorescence (excitation/emission ≈490/617 nm), shown in Figure 5B and Figure S24 (Supporting Information). A blind analytical study of cell viability was performed using ANOVA showed no significant differences between cells cultured with films and the control group. The in vitro biodegradation tests were performed by soaking the 3-layer SiON-PA films (3L-R2-50SSQ, 12 × 12 mm, thickness ≈100 µm) in PBS at a series of elevated temperatures, followed by observing the degradation process once per day under an optical microscope (VHX-6000 Series, Keyence) until the films completely dissolved.

In Vivo Biocompatibility and Biodegradation: All procedures associated with the animal studies followed the Guide for the Care and Use of Laboratory Animals of the National Institutes of Health and approved by The Institutional Animal Care and Use Committee at Northwestern University (Approval numbers: IS00018881 and IS00024102).

Female mice (C57/BL6; age at the initiation of the treatment: 8–12weeks; Charles River Laboratories) were anaesthetized using isoflurane gas (1–2% isoflurane in oxygen) in an anesthetizing chamber during the implantation surgery. The films under test were 3-layer SiON-PA films with the polymer composition R2-50SSQ-PA cut into a rectangular shape (5 × 10 mm, thickness ≈100 µm). After sterilizing in a steam sterilizer for 25 min at 121 °C (or by UV irradiation overnight), two films were implanted in the dorsal subcutaneous space of each mouse ($n = 9$) without overlapping between films. The sham group ($n = 4$), which served as a control, was subjected to the same surgery procedures but without film implantation. The incision was closed using interrupted sutures followed by standard combined postoperative analgesic regimen. The weights of the mice were recorded every week (Figure 5c). After 4 and 8 weeks, the mice with films implanted were euthanized to collect blood, organs, and tissues for subsequent blood, elemental, and histological analyses, referred to as the 4-week ($n = 4$) and 8-week group ($n = 5$), respectively. Mice in the sham group were euthanized at 8 weeks ($n = 4$).

To evaluate the distribution of Si resulting from film degradation, organs, including heart, spleen, kidney, brain, lung, and liver were collected and weighed (Figure 5d), and then dissolved in 50-mL tubes (metal-free, Thermo Fihser Scientific) using solutions of 500-µL HNO_3 and 125-µL H_2O_2 (volume fraction, HNO_3:H_2O_2 = 4:1), which were kept in a water bath at 65 °C until the organs were fully digested, and diluted with Millipore water to 10 mL after the solution cooled to room temperature. The solution was then analyzed by inductively coupled plasma optical emission spectrometry (ICP-OEX, iCAP 6500, Thermo Fisher Scientific). All measurements were performed simultaneously at three different wavelengths 212.412, 251.611, and 221.667 nm and the results presented here were obtained by averaging the values of these emission lines (Figure 5E).[48]

To assess the overall health of mice implanted with films, blood samples were collected and tested at the Veterinary Diagnostic Laboratory at University of Illinois. Blood was collected in collection tubes with K2-EDTA coatings and fully mixed with K2-EDTA to obtain the whole blood for CBC test. To obtain serum for blood chemistry tests, blood was collected in tubes without K2-EDTA coatings and centrifuged at 5000 rpm for 10 min after immersion in an ice bath for 5 min. The serum was transferred to a new tube using a pipette.

For histological studies, subcutaneous tissue and muscle were collected, fixed, and stored in formalin in 20-mL glass vials, followed by embedding in paraffin, sectioning, and staining with hematoxylin and eosin (H&E) at the Mouse Histology and Phenotyping Laboratory (MHPL) at Northwestern University. These tissue samples were observed using bright-field microscopy (VS120, Olympus). A blind histological assessment was performed, and representative images were shown in Figure 5H and Figure S25A (Supporting Information). Skin thickness and myofiber size were blindly analyzed using ANOVA, which showed no significant differences between film implantation groups and control groups, Figure 5I and Figure S25B (Supporting Information).

Device Fabrication and Measurements: The inductor–capacitor (LC) circuit consisted of laser-cut Zn coils (width: 100 µm) insulated by wax and then electrically connected with two Zn electrodes separated by a film of PLGA (thickness: 10 µm; lactide:glycolide, 50:50; molecular weight: 50 000–75 000) using a bioresorbable conductive wax paste.[37] The LC circuit was then placed on a glass slide, with the exposed side encapsulated by a 3-layer SiON-PA film. A PDMS tube positioned on top of the film with edges sealed using marine epoxy defined a structure to enable immersion in PBS solution, placed in an oven at 37 °C. The change in frequency of the LC circuit was monitored using a vector network analyzer (E5063A, Keysight, USA).

For the power receiving module, the fabrication began with laser-cutting to form a molybdenum coil from a foil (Mo, thickness: 100 µm; Goodfellow, USA) followed by removal of surface oxidation by immersion in aqua regia for 3–5 min. The next step involved separating the coils with PLGA films (thickness: 10 µm) and electrically connecting the coils and a LED with a bioresorbable conductive wax paste, with the system encapsulated by a 3-layer SiON-PA film. Test conditions were the same as those for the LC circuit. The RF behavior of the coils (S11 in dB) was evaluated using a vector network analyzer, to determine the peak frequency and quality factor (Q). A signal generator (3390, Keithley) provided RF power to a transmitter coil (60 mm diameter, 3 turns) placed over the coils to wirelessly power the LED.

The implantable LED devices used designs modified from flexible near-field wireless optoelectronic systems reported previously for optogenetics applications.[49] The device consisted of two circular Cu coils (diameter: 6 mm,10 turns; thickness: 18 µm; dielectric layer: 75-µm polyimide) with surface-mounted electronic components for power transfer. Power transfer uses magnetic coupling to a separate RF transmission loop antenna (a near-field communication (NFC) extension board, STMicroelectronics) or a wireless powering system (Optogenetics Starter Kit, NeuroLux, USA) operating at 13.56 MHz (Figure S26, Supporting Information). Device fabrication began with patterning a flexible substrate made of a copper–PI–copper laminate (Pyralux, DuPont, USA) using laser ablation (LPKF, ProtoLaser U4, Germany) to define the circuit interconnects and the bonding pads for the electronic components. These flexible printed circuit boards with customized designs can also be obtained from commercial vendors (i.e., PCBWay). Hot-air soldering indium solder bonded electronic components, including two diodes, one capacitor, and two LEDs with emission at 630 nm. The resonant frequency of devices was measured using a vector network analyzer (E5063A, Keysight) while LEDs were wirelessly powered by the NFC extension board or the wireless powering system.

Device encapsulation using SiON-PA films began with cutting 3-layer SiON-PA films into circular forms (diameter: 10 mm) using a CO_2 laser ablation system followed by deposition of SiO_2 (thickness: ≈30 nm) via sputtering (AJA Orion Sputter System, AJA International, Inc.) and UV/ozone (UVO) exposure of the SiO_2 for 3 min. The next steps included sandwiching a device between two SiON-PA films (the UVO-treated sides facing the device), applying silicon adhesive (Kwik-Sil, World Precision Instruments, USA) to the edges, and placing the setup in a hot-press machine, preset to a temperature of 35 °C, for 30 min. Applying epoxy (Loctite, USA) to seal the edges further prevented water permeation from those regions to complete the process.

Device Level Demonstration on Water Barrier Performance In Vivo: All procedures associated with the animal studies followed the Guide for the Care and Use of Laboratory Animals of the National Institutes of Health and approved by The Institutional Animal Care and Use Committee at Northwestern University (Approval numbers: IS00018881 and IS00024102). Female mice (C57/BL6; age at the initiation of the treatment: 8–12 weeks; Charles River Laboratories) were anaesthetized using isoflurane gas (1–2% isoflurane in oxygen) in an anesthetizing chamber before the implantation surgery. After sterilizing by UV irradiation for 2 h, three optoelectronic devices that were encapsulated using the 3-layer SiON-PA films underwent subcutaneous implantation ($n = 3$). Mice in the sham group ($n = 3$) were subjected to the same surgery procedures, but the

implanted devices lacked film encapsulation. The incision was closed using interrupted sutures followed by standard combined postoperative analgesic regimen. After a designated implantation period, the mice both in the implantation and the sham groups were anaesthetized to collect data on resonant frequency of the implanted devices and LED illumination conditions. One mouse was sacrificed to harvest the device at the 3-week timepoint to provide a visual examination of the device and the encapsulation films.

Statistical Analysis: Results present as mean ± standard deviation with $n \geq 3$. The ordinary one-way ANOVA with post hoc Tukey's means comparisons ($p < 0.05$) was used for statistical significance testing for histological analysis. GraphPad Prism and/or Origin software were used to perform statistical analysis. ImageJ software was used for grayscale analysis of images.

Supporting Information

Supporting Information is available from the Wiley Online Library or from the author.

Acknowledgements

Z.H., H.G., and D.A. contributed equally to this work. This work was supported by the Querrey Simpson Institute for Bioelectronics. The authors specially thank Dr. Luyi Sun, Zaili Hou at University of Connecticut, Dr. Hui Fang at Dartmouth College, and Dr. Cunjiang Yu, Dr. Zhoulyu Rao, and Yuntao Lu at Pennsylvania State University for helpful discussions. This work utilized Northwestern University Micro/Nano Fabrication Facility (NUFAB), Keck Interdisciplinary Surface Science facility (Keck-II), Scanned Probe Imaging and Development (SPID) facility of Northwestern University's NUANCE Center, which has received support from Soft and Hybrid Nanotechnology Experimental (SHyNE) Resource (NSF ECCS-2025633), the IIN, and Northwestern's MRSEC program (NSF DMR-1720139). Histology services were provided by the Northwestern University Mouse Histology and Phenotyping Laboratory which is supported by NCI P30-CA060553 awarded to the Robert H. Lurie Comprehensive Cancer Center. The authors thank Dr. Elizabeth Dempsey for the help with the studies on CBC and blood chemistry. Film transparency characterizations were performed at Keck Biophysics Facility by Eleanor Dunietz. Si elemental distribution was measured at Quantitative Bio-element Imaging Center by Rebecca A. Sponenburg. This work also made use of the IMSERC Physical Characterization facility at Northwestern University, which has received support from SHyNE Resource (NSF ECCS-2025633), and Northwestern University, the MatCI Facility supported by the MRSEC program of the National Science Foundation (DMR-1720139) at the Materials Research Center of Northwestern University, and NU-LED core facility. Ther authors acknowledge Dr. Christos D. Malliakas, Dr. Stephen Miller, and Carla J. Shute for their help with the equipment. R.L. acknowledges the support from the National Natural Science Foundation of China (grants 12022209 and 11972103). B.W. acknowledges the support from the National Natural Science Foundation of China (grant 11825202 and U21A20429).

Conflict of Interest

The authors declare no conflict of interest.

Data Availability Statement

The data that support the findings of this study are available in the supplementary material of this article.

Keywords

biofluid barriers, bioresorbable electronics, electronics packaging, organic–inorganic materials

Received: September 12, 2023
Revised: January 31, 2024
Published online: February 27, 2024

[1] Y. M. Zhang, G. M. Lee, S. Li, Z. Y. Hu, K. Y. Zhao, J. A. Rogers, *Chem. Rev.* **2023**, *123*, 11722.
[2] J. Koo, M. R. MacEwan, S. K. Kang, S. M. Won, M. Stephen, P. Gamble, Z. Q. Xie, Y. Yan, Y. Y. Chen, J. Shinetc, J. A. Rogers, *Nat. Med.* **2018**, *24*, 1830.
[3] G. Yao, L. Kang, C. C. Li, S. H. Chen, Q. Wang, J. Z. Yang, Y. Long, J. Li, K. N. Zhao, W. N. Xuetc, X. D. Wang, *Proc. Natl. Acad. Sci. U. S. A.* **2021**, *118*, e2100772118.
[4] S. W. Hwang, H. Tao, D. H. Kim, H. Y. Cheng, J. K. Song, E. Rill, M. A. Brenckle, B. Panilaitis, S. M. Won, Y. S. Kim, Y. M. Song, K. J. Yu, A. Ameen, R. Li, Y. W. Su, M. M. Yang, D. L. Kaplan, M. R. Zakin, M. J. Slepian, Y. G. Huang, F. G. Omenetto, J. A. Rogers, *Science* **2012**, *337*, 1640.
[5] C. M. Li, C. C. Guo, V. Fitzpatrick, A. Ibrahim, M. J. Zwierstra, P. Hanna, A. Lechtig, A. Nazarian, S. J. Lin, D. L. Kaplan, *Nat. Rev. Mater.* **2020**, *5*, 61.
[6] W. B. Han, J. H. Lee, J. W. Shin, S. W. Hwang, *Adv. Mater.* **2020**, *32*, 2002211.
[7] X. W. Yu, W. Shou, B. K. Mahajan, X. Huang, H. Pan, *Adv. Mater.* **2018**, *30*,1707624.
[8] S. K. Kang, R. K. J. Murphy, S. W. Hwang, S. M. Lee, D. V. Harburg, N. A. Krueger, J. H. Shin, P. Gamble, H. Y. Cheng, S. Yu, Z. J. Liu, J. G. McCall, M. Stephen, H. Z. Ying, J. Kim, G. Park, R. C. Webb, C. H. Lee, S. J. Chung, D. S. Wie, A. D. Gujar, B. Vemulapalli, A. H. Kim, K. M. Lee, J. J. Cheng, Y. G. Huang, S. H. Lee, P. V. Braun, W. Z. Ray, J. A. Rogers, *Nature* **2016**, *530*, 71.
[9] K. J. Yu, D. Kuzum, S. W. Hwang, B. H. Kim, H. Juul, N. H. Kim, S. M. Won, K. Chiang, M. Trumpis, A. G. Richardson, H. Y. Cheng, H. Fang, M. Thompson, H. Bink, D. Talos, K. J. Seo, H. N. Lee, S. K. Kang, J. H. Kim, J. Y. Lee, Y. G. Huang, F. E. Jensen, M. A. Dichter, T. H. Lucas, J. Viventi, B. Litt, J. A. Rogers, *Nat. Mater.* **2016**, *15*, 782.
[10] Y. S. Choi, H. Jeong, R. T. Yin, R. Avila, A. Pfenniger, J. Yoo, J. Y. Lee, A. Tzavelis, Y. J. Lee, S. W. Chen, H. S. Knight, S. Kim, H. Y. Ahn, G. Wickerson, A. Vazquez-Guardado, E. Higbee-Dempsey, B. A. Russo, M. A. Napolitano, T. J. Holleran, L. A. Razzak, A. N. Miniovich, G. Lee, B. Geist, B. Kim, S. Han, J. A. Brennan, K. Aras, S. S. Kwak, J. Kim, E. A. Waters, et al., *Science* **2022**, *376*, 1006.
[11] J. Koo, S. B. Kim, Y. S. Choi, Z. Q. Xie, A. J. Bandodkar, J. Khalifeh, Y. Yan, H. Kim, M. K. Pezhouh, K. Doty, G. Lee, Y. Y. Chen, S. M. Lee, D. D'Andrea, K. Jung, K. Lee, K. Li, S. Jo, H. L. Wang, J. H. Kim, J. Kim, S. G. Choi, W. J. Jang, Y. S. Oh, I. Park, S. S. Kwak, J. H. Park, D. Hong, X. Feng, C. H. Lee, et al., *Sci. Adv.* **2020**, *6*, eabb1093.
[12] Y. S. Choi, R. T. Yin, A. Pfenniger, J. Koo, R. Avila, K. B. Lee, S. W. Chen, G. Lee, G. Li, Y. Qiao, A. Murillo-Berlioz, A. Kiss, S. L. Han, S. M. Lee, C. H. Li, Z. Q. Xie, Y. Y. Chen, A. Burrell, B. Geist, H. Jeong, J. Kim, H. J. Yoon, A. Banks, S. K. Kang, Z. J. Zhang, C. R. Haney, A. V. Sahakian, D. Johnson, T. Efimova, Y. G. Huang, et al., *Nat. Biotechnol.* **2021**, *39*, 1228.
[13] Y. Gao, Y. Zhang, X. Wang, K. Sim, J. S. Liu, J. Chen, X. Feng, H. X. Xu, C. J. Yu, *Sci. Adv.* **2017**, *3*, e1701222.
[14] J. T. Reeder, Z. Xie, Q. Yang, M. H. Seo, Y. Yan, Y. Deng, K. R. Jinkins, S. R. Krishnan, C. Liu, S. McKay, E. Patnaude, A. Johnson, Z. Zhao, M. J. Kim, Y. Xu, I. Huang, R. Avila, C. Felicelli, E. Ray, X. Guo, W. Z. Ray, Y. Huang, M. R. MacEwan, J. A. Rogers, *Science* **2022**, *377*, 109.
[15] S. M. Won, J. Koo, K. E. Crawford, A. D. Mickle, Y. G. Xue, S. Min, L. A. McIlvried, Y. Yan, S. B. Kim, S. M. Lee, B. H. Kim, H. Jang, M. R.

MacEwan, Y. G. Huang, R. W. Gereau, J. A. Rogers, *Adv. Funct. Mater.* **2018**, *28*, 1801819.
[16] Z. Q. Fang, H. L. Zhang, S. Y. Qiu, Y. Kuang, J. Zhou, Y. Lan, C. Sun, G. H. Li, S. Q. Gong, Z. Q. Ma, *Adv. Mater. Technol.* **2021**, *6*, 2000928.
[17] Q. S. Yang, S. Lee, Y. G. Xue, Y. Yan, T. L. Liu, S. K. Kang, Y. J. Lee, S. H. Lee, M. H. Seo, D. Lu, J. Koo, M. R. MacEwan, R. S. T. Yin, W. Z. Ray, Y. G. Huang, J. A. Rogers, *Adv. Funct. Mater.* **2020**, *30*, 1910718.
[18] J. H. Shin, Y. Yan, W. B. Bai, Y. G. Xue, P. Gamble, L. M. Tian, I. Kandela, C. R. Haney, W. Spees, Y. Lee, M. Choi, J. Ko, H. Ryu, J. K. Chang, M. Pezhouh, S. K. Kang, S. M. Won, K. J. Yu, J. N. Zhao, Y. K. Lee, M. R. MacEwan, S. K. Song, Y. G. Huang, W. Z. Ray, J. A. Rogers, *Nat. Biomed. Eng.* **2019**, *3*, 37.
[19] E. M. Song, H. Fang, X. Jin, J. N. Zhao, C. S. Jiang, K. J. Yu, Y. D. Zhong, D. Xu, J. H. Li, G. H. Fang, H. N. Du, J. Z. Zhang, J. M. Park, Y. G. Huang, M. A. Alam, Y. F. Mei, J. A. Rogers, *Adv. Electron. Mater.* **2017**, *3*, 1700077.
[20] H. I. Lee, J. B. Park, W. Xianyu, K. Kim, J. G. Chung, Y. K. Kyoung, S. Byun, W. Y. Yang, Y. Y. Park, S. M. Kim, E. Cho, J. K. Shin, *Sci. Rep.* **2017**, *7*, 14146.
[21] Y. Shi, L. He, F. C. Guang, L. H. Li, Z. Q. Xin, R. P. Liu, *Micromachines* **2019**, *10*, 552.
[22] H. Fang, J. N. Zhao, K. J. Yu, E. M. Song, A. B. Farimani, C. H. Chiang, X. Jin, Y. G. Xue, D. Xu, W. B. Du, K. J. Seo, Y. D. Zhong, Z. J. Yang, S. M. Won, G. H. Fang, S. W. Choi, S. Chaudhuri, Y. G. Huang, M. A. Alam, J. Viventi, N. R. Aluru, J. A. Rogers, *Proc. Natl. Acad. Sci. U. S. A.* **2016**, *113*, 11682.
[23] M. Mariello, K. Kim, K. Wu, S. P. Lacour, Y. Leterrier, *Adv. Mater.* **2022**, *34*, 2201129.
[24] S. K. Kang, S. W. Hwang, H. Y. Cheng, S. Yu, B. H. Kim, J. H. Kim, Y. G. Huang, J. A. Rogers, *Adv. Funct. Mater.* **2014**, *24*, 4427.
[25] A. Göpferich, J. Tessmar, *Adv. Drug Delivery Rev.* **2002**, *54*, 911.
[26] Y. S. Choi, J. Koo, Y. J. Lee, G. Lee, R. Avila, H. Z. Ying, J. Reeder, L. Hambitzer, K. Im, J. Kim, K. M. Lee, J. J. Cheng, Y. G. Huang, S. K. Kang, J. A. Rogers, *Adv. Funct. Mater.* **2020**, *30*, 2000941.
[27] K. M. Schreck, D. Leung, C. N. Bowman, *Macromolecules* **2011**, *44*, 7520.
[28] H. Lin, X. Wan, X. S. Jiang, Q. K. Wang, J. Yin, *Adv. Funct. Mater.* **2011**, *21*, 2960.
[29] A. Hezi-Yamit, C. Sullivan, J. Wong, L. David, M. F. Chen, P. W. Cheng, D. Shumaker, J. N. Wilcox, K. Udipi, *J. Biomed. Mater. Res. A* **2009**, *90a*, 133.
[30] J. Shin, Z. H. Liu, W. B. Bai, Y. H. Liu, Y. Yan, Y. G. Xue, I. Kandela, M. Pezhouh, M. R. MacEwan, Y. G. Huang, W. Z. Ray, W. D. Zhou, J. A. Rogers, *Sci. Adv.* **2019**, *5*, eaaw1899.
[31] T. W. Kim, M. Yan, A. G. Erlat, P. A. McConnelee, M. Pellow, J. Deluca, T. P. Feist, A. R. Duggal, M. Schaepkens, *J. Vac. Sci. Technol. A* **2005**, *23*, 971.
[32] G. L. Graff, R. E. Williford, P. E. Burrows, *J. Appl. Phys.* **2004**, *96*, 1840.
[33] J. Wu, F. Fei, C. Wei, X. Chen, S. Nie, D. Zhang, W. Su, Z. Cui, *RSC Adv.* **2018**, *8*, 5721.
[34] N. G. March, E. J. Carr, *J. Comput. Appl. Math.* **2019**, *345*, 206.
[35] E. J. Carr, N. G. March, *Appl. Math. Comput.* **2018**, *333*, 286.
[36] H. Yuk, C. E. Varela, C. S. Nabzdyk, X. Mao, R. F. Padera, E. T. Roche, X. Zhao, *Nature* **2019**, *575*, 169.
[37] D. Lu, Y. Yan, Y. J. Deng, Q. S. Yang, J. Zhao, M. H. Seo, W. B. Bai, M. R. MacEwan, Y. G. Huang, W. Z. Ray, J. A. Rogers, *Adv. Funct. Mater.* **2020**, *30*, 2003754.
[38] D. Lu, Y. Yan, R. Avila, I. Kandela, I. Stepien, M. H. Seo, W. B. Bai, Q. S. Yang, C. H. Li, C. R. Haney, E. A. Waters, M. R. MacEwan, Y. G. Huang, W. Z. Ray, J. A. Rogers, *Adv. Healthcare Mater.* **2020**, *9*, e2000942.
[39] G. T. Hwang, D. Im, S. E. Lee, J. Lee, M. Koo, S. Y. Park, S. Kim, K. Yang, S. J. Kim, K. Lee, K. J. Lee, *ACS Nano* **2013**, *7*, 4545.
[40] J. M. T. Gere, S. P. Timoshenko, *Mechanics of Materials*, Springer US, Boston, MA, **1991**.
[41] Z. H. Gan, C. Z. Wang, Z. Chen, *Surfaces* **2018**, *1*, 59.
[42] M. Jozwik, P. Delobelle, C. Gorecki, A. Sabac, L. Nieradko, C. Meunier, F. Munnik, *Thin Solid Films* **2004**, *468*, 84.
[43] G. Carlotti, P. Colpani, D. Piccolo, S. Santucci, V. Senez, G. Socino, L. Verdini, *Thin Solid Films* **2002**, *414*, 99.
[44] G. N. Greaves, A. L. Greer, R. S. Lakes, T. Rouxel, *Nat. Mater.* **2011**, *10*, 823.
[45] A. Muller, M. C. Wapler, U. Wallrabe, *Soft Matter* **2019**, *15*, 779.
[46] R. Li, H. T. Cheng, Y. W. Su, S. W. Hwang, L. Yin, H. Tao, M. A. Brenckle, D. H. Kim, F. G. Omenetto, J. A. Rogers, Y. G. Huang, *Adv. Funct. Mater.* **2013**, *23*, 3106.
[47] S. Hauptkorn, J. Pavel, H. Seltner, *Fresenius J. Anal. Chem.* **2001**, *370*, 246.
[48] G. Shin, A. M. Gomez, R. Al-Hasani, Y. R. Jeong, J. Kim, Z. Xie, A. Banks, S. M. Lee, S. Y. Han, C. J. Yoo, J. L. Lee, S. H. Lee, J. Kurniawan, J. Tureb, Z. Guo, J. Yoon, S. I. Park, S. Y. Bang, Y. Nam, M. C. Walicki, V. K. Samineni, A. D. Mickle, K. Lee, S. Y. Heo, J. G. McCall, T. Pan, L. Wang, X. Feng, T. I. Kim, J. K. Kim, et al., *Neuron* **2017**, *93*, 509.
[49] P. V. Danckwerts, *Trans. Faraday Soc.* **1950**, *46*, 300.